

Electronic Supplementary Information for

Low-temperature Transport Properties of the *n*-type Layered Homologous Compounds



Pavan Kumar-Ventrapati¹, Shantanu Misra¹, Gaëlle Delaizir², Anne Dauscher¹, Bertrand Lenoir¹ and Christophe Candolfi^{1,*}

¹ *Institut Jean Lamour, UMR 7198 CNRS – Université de Lorraine, 2 allée André Guinier – Campus ARTEM, 54000 Nancy, France*

² *Sciences des Procédés Céramique et de Traitement de Surface (SPCTS), UMR CNRS 7315- Université de Limoges, Limoges, France*

*Corresponding author: christophe.candolfi@univ-lorraine.fr

Content

Figure S1. Optical absorption spectra of the $x = 0.0, 1.2$ and 2.4 samples plotted for indirect transitions.

Figure S2. Comparison of the temperature dependences of the Hall coefficient R_H of the binary Bi_8Se_7 measured parallel and perpendicular to the pressing direction.

Experimental details for the high-temperature thermoelectric properties measurements

Figures S3. Comparison of the temperature dependence of the electrical resistivity ρ measured parallel and perpendicular to the pressing direction.

Figures S4. Comparison of the temperature dependence of the thermopower α measured parallel and perpendicular to the pressing direction.

Figure S5. Temperature dependences of the electrical resistivity ρ , thermopower α and power factor α^2/ρ at low and high temperatures.

Figure S6. Comparison of the temperature dependences of the total thermal conductivity κ measured parallel and perpendicular to the pressing direction.

Figure S7. Low- and high-temperature dependences of the total thermal conductivity κ and lattice thermal conductivity κ_{ph} .

Figure S8. Low- and high-temperature dependence of the dimensionless thermoelectric figure of merit ZT .

Figure S9. Comparison of the temperature dependences of the dimensionless thermoelectric figure of merit ZT measured parallel and perpendicular to the pressing direction.

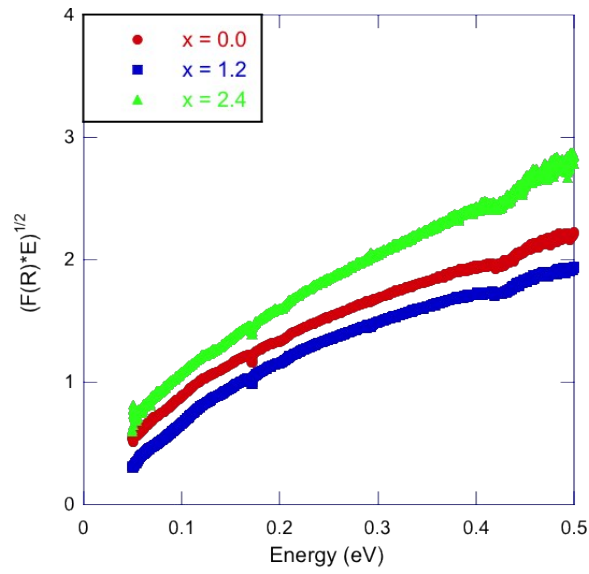


Figure S1. Optical absorption spectra of the $x = 0.0$, 1.2 and 2.4 samples plotted as $[F(R) \times E]^{1/2}$ as a function of the energy E assuming indirect transitions. The intercept of the low-energy curves with the x axis, indicative of the width of a possible band gap, would be consistent with either semi-metallic states or narrow-band-gap semiconducting states. Slightly above 0.4 eV, another optical transition is observed.

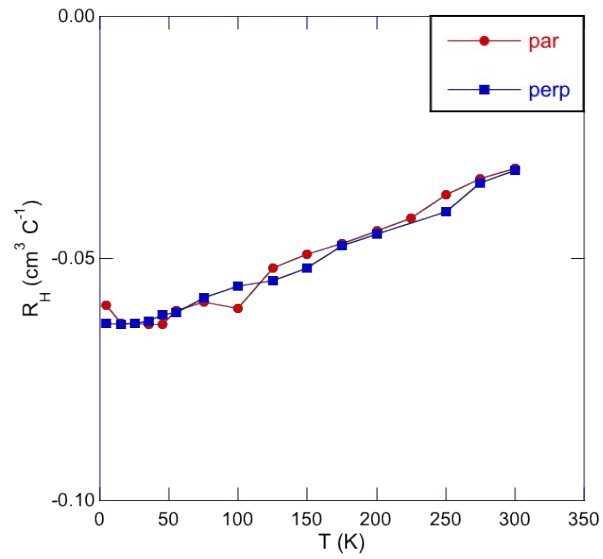


Figure S2. Comparison of the temperature dependences of the Hall coefficient R_H of Bi_8Se_7 measured parallel and perpendicular to the pressing direction.

Experimental details for the high-temperature thermoelectric properties measurements

Electrical resistivity and thermopower were measured simultaneously on bar-shaped samples (typical dimensions of $1.5 \times 1.5 \times 7 \text{ mm}^3$) at high temperatures (300 – 700 K) under an inert He atmosphere using a ZEM-3 instrument (Ulvac-Riko). The thermal conductivity was determined in the same temperature range via thermal diffusivity a measurements, performed by a laser flash technique using a LFA 427 instrument (Netzsch). These measurements were realized on graphite-coated disc-shaped samples (10 mm in diameter and 1 mm in thickness). Thermal conductivity was then calculated according to the relation $\kappa = aC_p d$ where d is the experimental density and C_p is the specific heat. The temperature dependence of the density has been neglected in the present case. The theoretical density used in these calculations has been determined from X-ray diffraction data to vary between 8.38 for $x = 0.0$ to 8.57 g cm^{-3} for $x = 2.4$. The specific heat was approximated by the Dulong-Petit law $C_p = 3NR$ where N is the number of atoms per formula unit and R is the ideal gas constant.

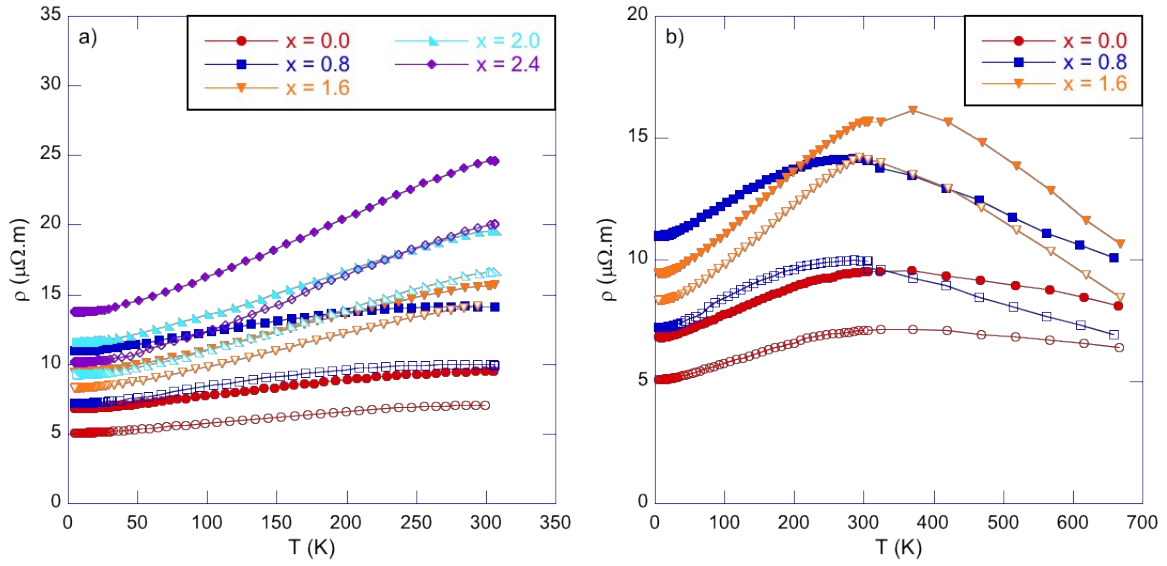


Figure S3. a) Comparison of the low-temperature temperature dependences of the electrical resistivity ρ of the $\text{Bi}_{8-x}\text{Sb}_x\text{Se}_7$ samples for $x = 0.0, 0.8, 1.6, 2.0$ and 2.4 . Open and filled symbols correspond to data measured perpendicular and parallel to the pressing direction, respectively. b) Comparison of the temperature dependences of the electrical resistivity ρ of the $\text{Bi}_{8-x}\text{Sb}_x\text{Se}_7$ samples. For sake of clarity, only the data for $x = 0.0, 0.8$ and 1.6 are shown.

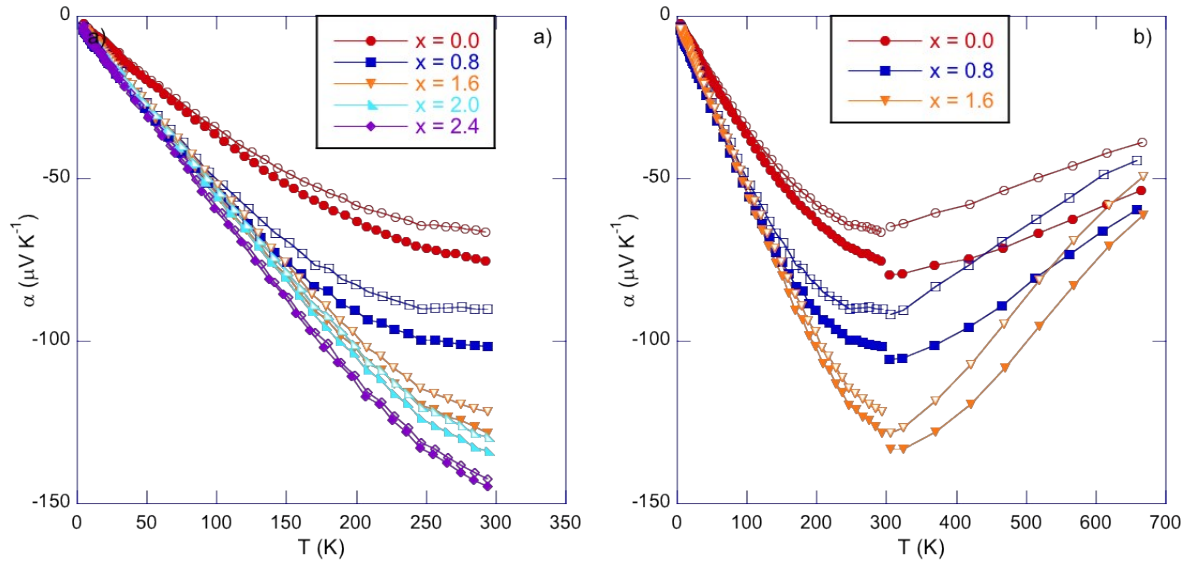


Figure S4. a) Comparison of the low-temperature temperature dependences of the thermopower α of the $\text{Bi}_{8-x}\text{Sb}_x\text{Se}_7$ samples for $x = 0.0, 0.8, 1.6, 2.0$ and 2.4 . Open and filled symbols correspond to data measured perpendicular and parallel to the pressing direction, respectively. b) Comparison of the temperature dependences of the thermopower α of the $\text{Bi}_{8-x}\text{Sb}_x\text{Se}_7$ samples. For sake of clarity, only the data for $x = 0.0, 0.8$ and 1.6 are shown.

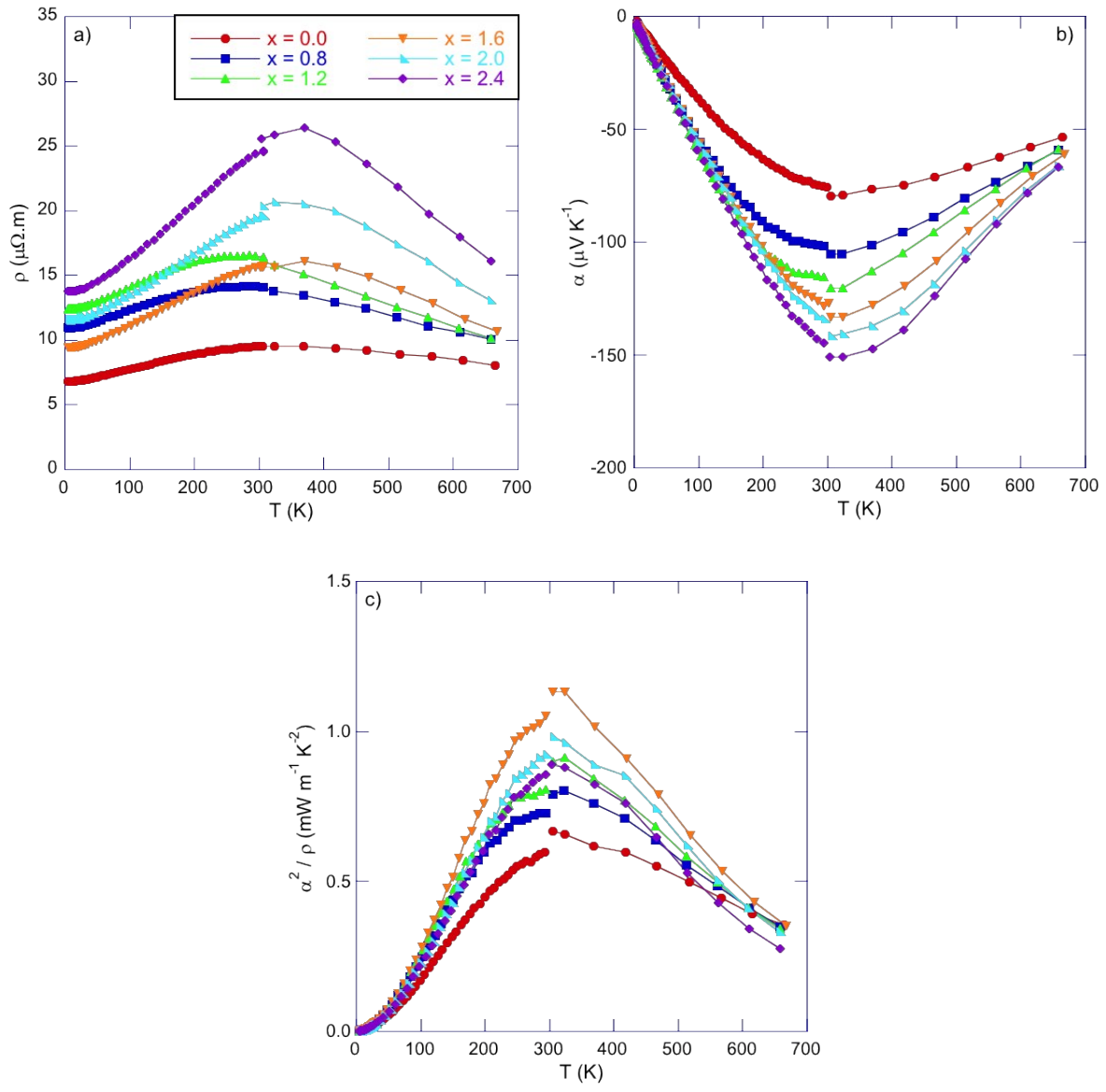


Figure S5. Temperature dependences of the low- and high-temperature a) electrical resistivity ρ , b) thermopower α and c) power factor α^2/ρ for the series for the series $\text{Bi}_{8-x}\text{Sb}_x\text{Se}_7$ ($0.0 \leq x \leq 2.4$). The color-coded symbols are similar in the three panels.

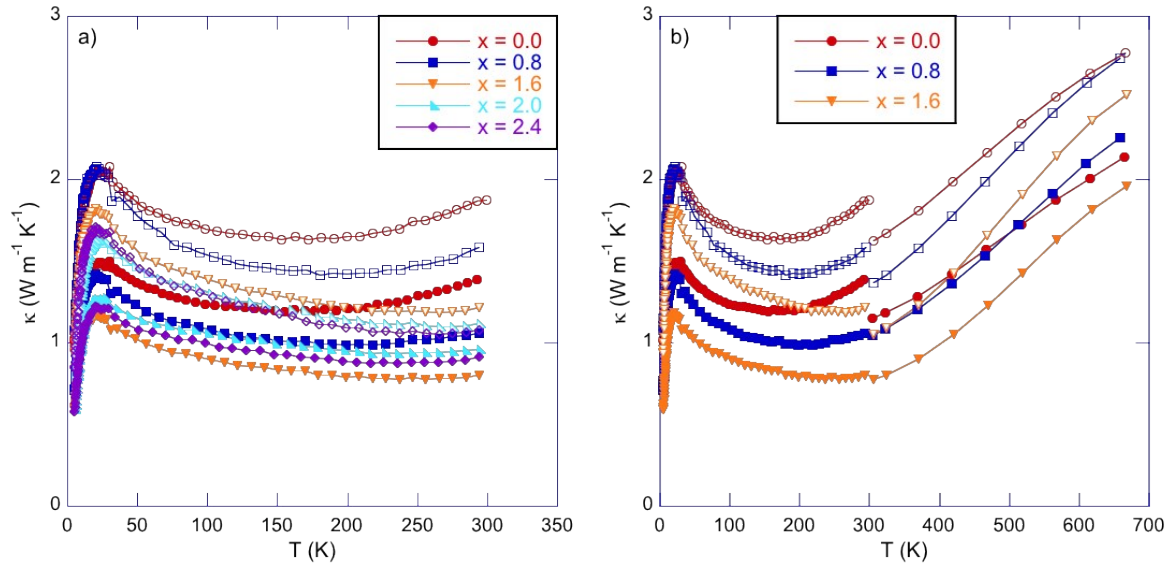


Figure S6. a) Comparison of the low-temperature temperature dependences of the total thermal conductivity κ of the $\text{Bi}_{8-x}\text{Sb}_x\text{Se}_7$ samples for $x = 0.0, 0.8, 1.6, 2.0$ and 2.4 . Open and filled symbols correspond to data measured perpendicular and parallel to the pressing direction, respectively. b) Comparison of the temperature dependences of the total thermal conductivity κ of the $\text{Bi}_{8-x}\text{Sb}_x\text{Se}_7$ samples. For sake of clarity, only the data for $x = 0.0, 0.8$ and 1.6 are shown. The mismatch observed between the low- and high-temperature data sets at 300 K is due to the thermal radiations that accompany the low-temperature measurements and increase the measured values.

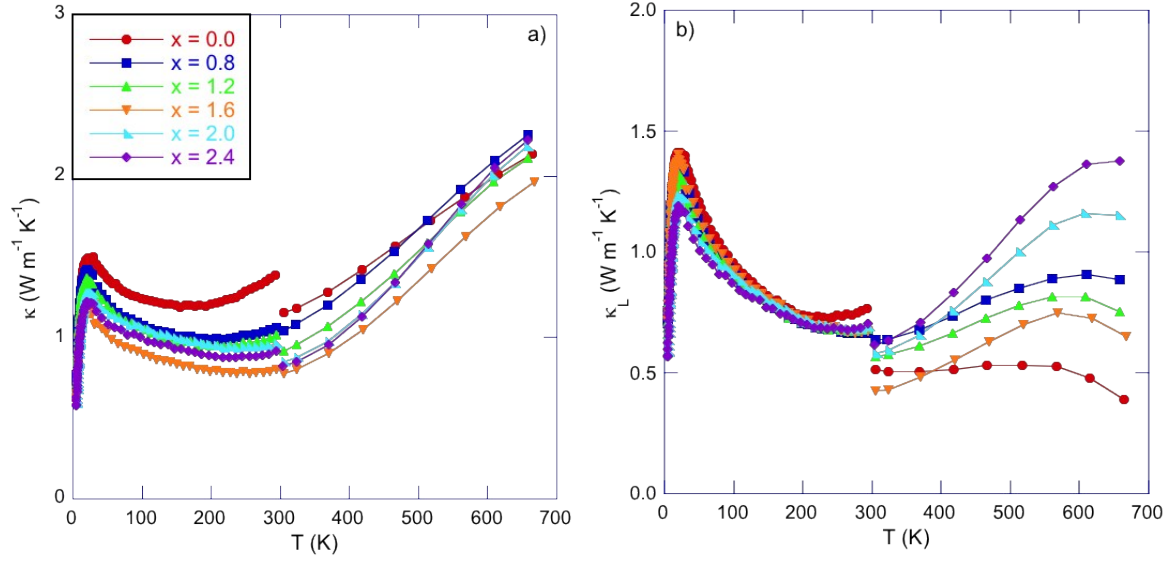


Figure S7. Low- and high-temperature dependences of the a) total thermal conductivity κ and b) lattice thermal conductivity κ_L for the series $\text{Bi}_{8-x}\text{Sb}_x\text{Se}_7$ ($0.0 \leq x \leq 2.4$). The color-coded symbols are similar in both panels. The mismatch observed at 300 K between the low and high-temperature κ values is due to the contribution of thermal radiations that accompany the low-temperature measurements. At high temperatures, the increase observed in κ_L is due to the bipolar contribution stemming from the thermal excitation of minority carriers. This effect, observed only above 550 K in the binary sample due to its stronger degenerate nature, is more pronounced for $x \geq 2.0$. Regardless of the Sb content, the overall temperature dependence observed is consistent with the thermal excitation of minority carriers evidenced in both $\alpha(T)$ and $\rho(T)$, which gives rise to a bipolar contribution to $\kappa(T)$ above 300 K. Note that the electron-hole pairs dominating the transport above 300 K results in L values artificially higher than those determined by the SPB model (see *e.g.* Ö. Ceyda Yelgel and G. P. Srivastava, *Phys. Rev. B*, 2012, **85**, 125207).

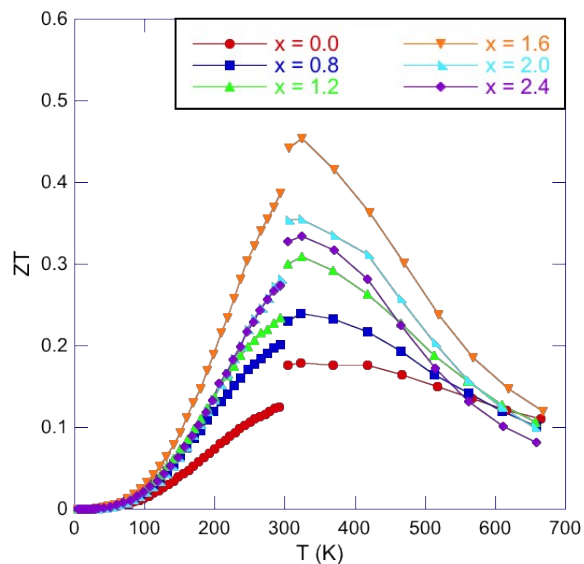


Figure S8. Low- and high-temperature dependence of the dimensionless thermoelectric figure of merit ZT for the series $\text{Bi}_{8-x}\text{Sb}_x\text{Se}_7$ ($0.0 \leq x \leq 2.4$). The mismatch observed near 300 K between the low and high-temperature data sets is due to the thermal radiations accompanying the low-temperature thermal conductivity measurements.

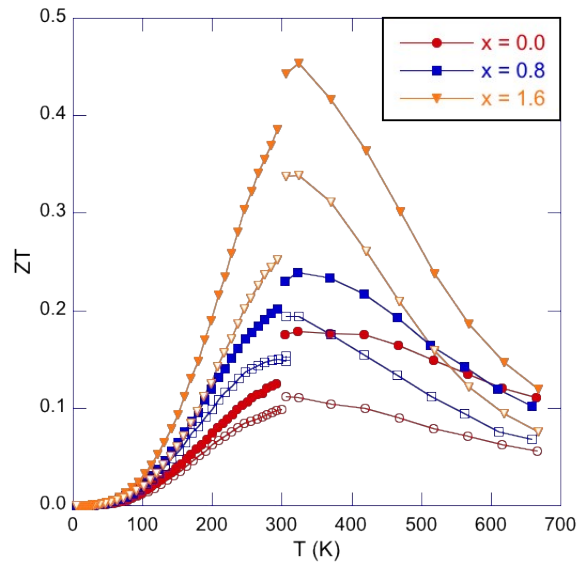


Figure S9. Comparison of the temperature dependences of the dimensionless thermoelectric figure of merit ZT of the $\text{Bi}_{8-x}\text{Sb}_x\text{Se}_7$ samples measured parallel and perpendicular to the pressing direction. Open and filled symbols correspond to data measured perpendicular and parallel to the pressing direction, respectively. For sake of clarity, only the data for $x = 0.0, 0.8$ and 1.6 are shown. The mismatch observed between the low- and high-temperature data sets at 300 K is due to the higher thermal conductivity values measured at low temperatures due to the parasitic contribution of thermal radiations.